Higher representations on the lattice: Numerical simulations, SU(2) with adjoint fermions

Luigi Del Debbio,[1] Agostino Patella,[2] and Claudio Pica[3,4]

[1]*SUPA, School of Physics and Astronomy, University of Edinburgh, Edinburgh EH9 3JZ, Scotland, United Kingdom*[*]

[2]*School of Physics, Swansea University, Swansea SA2 8PP, Wales, United Kingdom*[†]

[3]*CP*^{3}*-Origins, University of Southern Denmark, Odense, 5230 M, Denmark*[‡]

[4]*Physics Department, Brookhaven National Laboratory, Upton, New York 11973-5000, USA*

(Received 31 March 2010; published 20 May 2010)

We discuss the lattice formulation of gauge theories with fermions in arbitrary representations of the color group and present in detail the implementation of the hybrid Monte Carlo (HMC)/rational HMC algorithm for simulating dynamical fermions. We discuss the validation of the implementation through an extensive set of tests and the stability of simulations by monitoring the distribution of the lowest eigenvalue of the Wilson-Dirac operator. Working with two flavors of Wilson fermions in the adjoint representation, benchmark results for realistic lattice simulations are presented. Runs are performed on different lattice sizes ranging from $4^3 \times 8$ to $24^3 \times 64$ sites. For the two smallest lattices we also report the measured values of benchmark mesonic observables. These results can be used as a baseline for rapid cross-checks of simulations in higher representations. The results presented here are the first steps toward more extensive investigations with controlled systematic errors, aiming at a detailed understanding of the phase structure of these theories, and of their viability as candidates for strong dynamics beyond the standard model.

DOI: 10.1103/PhysRevD.81.094503 PACS numbers: 11.15.Ha, 12.60.Nz

I. INTRODUCTION

Recent algorithmic progress in simulations of QCD with dynamical fermions have shown that current computing facilities can reach beyond the quenched approximation without compromising the robustness of the formulation [1–6]. Besides their great relevance for lattice QCD, these improvements allow numerical simulations to be used as a quantitative, nonperturbative tool to study more generic strongly interacting theories where the role of the fermion determinant is crucial: extensive Monte Carlo studies will enable one to tame the systematic errors and therefore to obtain reliable information about the strong dynamics of theories beyond QCD. Examples that have a direct impact on physics beyond the standard model (BSM) include technicolor models [7,8] (see [9,10] for reviews), orientifold theories [11], and supersymmetry (see [12] for a recent review on the nonperturbative formulation of supersymmetry). Moreover the theoretical progresses in formulating QCD on the lattice provide the necessary tools for rigorous studies of BSM nonperturbative phenomena. This is of paramount importance in order to obtain reliable results as we move into the unknown territories of strongly interacting BSM theories: the clean field–theoretical framework developed for QCD needs to be exported to the studies of BSM strong dynamics in order to obtain lattice results that are trustable and therefore can have an impact on the LHC phenomenology.

Simulations of the theories listed above share a common technical challenge: they all require fermion fields in representations larger than the fundamental, gauge groups SU(N) with generic number of colors N, or a combination of both. Therefore a central ingredient of these simulations is a generalized Dirac operator that can act on vectors of arbitrary dimension in color space. We developed such an operator and tested its inversion in a recent study of the quenched meson spectrum in the large-N limit of pure Yang-Mills theories [13]. The same computational framework has also been used to assess the validity of the planar orientifold equivalence by numerical simulations in the quenched approximation [14].

Theories with two Dirac fermions in the two-index symmetric representation and small number of colors ($N = 2, 3$) are currently under scrutiny as viable candidates for strongly interacting BSM candidates [15–17]. An important feature of these theories is that the number of fermions is close to the critical value where an IR conformal fixed point may appear [18]. The vicinity of the IR fixed point can induce a walking behavior of the running coupling, which would make such theories phenomenologically viable. Whether or not this is really the case beyond perturbation theory can only be established by numerical simulations of such theories defined on the lattice. Recent studies of the running of the renormalized coupling in the Schrödinger functional (SF) scheme [19] with fundamental staggered fermions have provided first evidence of the existence of a conformal fixed point for $n_f = 12$ [20]. A similar study has also appeared for the SU(3) theory with fermions in the two-index symmetric representation [21], and for the SU(2) theory with fermions

[*]luigi.del.debbio@ed.ac.uk
[†]a.patella@swan.ac.uk
[‡]pica@cp3.sdu.dk

in the adjoint representation [22,23]. The results presented in those works confirm that the SF is indeed a valuable tool to study the RG structure of the theories under consideration. Further studies on the existence of an IR fixed point with fundamental fermions have appeared in the literature [24]. Several complementary approaches will be needed in order to fully understand numerical simulations in the vicinity of an IR fixed point.

In this paper we discuss in detail the implementation of an algorithm for simulating gauge theories with dynamical Wilson fermions in an arbitrary representation, and arbitrary gauge group SU(N), and present the results of preliminary runs which are useful as a benchmark for future simulations. At this stage in our investigations, the emphasis is on the algorithm rather than the optimization or the phenomenological results. Section II summarizes the notation used for the Dirac operator and introduces the conventions to deal with the higher representations. The hybrid Monte Carlo (HMC) algorithm for two flavors is described in Sec. III A. In order to be able to simulate theories with an arbitrary number of flavors, the rational HMC (RHMC) algorithm [6] has also been developed, as described in Sec. III B. Let us emphasize once again that, as numerical simulations move away from the well-known realms of QCD, we find it necessary to have a robust field–theoretical formulation and a tight control over the behavior of the numerical simulations. These are necessary conditions if numerical simulations want to be in a position to test candidate theories for strong electroweak symmetry breaking with any degree of confidence.

We study the behavior of the algorithm at different points in the space of bare lattice couplings by monitoring the time history, the probability distribution and the correlation time of the plaquette, and the lowest eigenvalue of the Dirac operator, in Sec. IV. In the same section we also study how the force is split in the terms of the rational approximation, in analogy with Ref. [6] where fundamental fermions were considered. We present results for $4^3 \times 8$, $8^3 \times 16$, $12^3 \times 24$, $16^3 \times 32$, $24^3 \times 64$ lattices, for the SU(2) theory with two flavors in the adjoint representation at two values of the coupling constant $\beta = 2$ and $\beta = 2.25$. The emphasis in this work is on the details of the implementation and on the behavior of the algorithm for the theory under consideration. These results are intended as a benchmark for other softwares that simulate the same theory. When the exactness of numerical simulations cannot be judged by comparing with experimental data, a cross-check of all the available simulation softwares is essential before debating about the interpretation of the results. Up to date this preliminary cross-check is still missing, although several more complex and phenomenologically relevant results are currently available in the literature [22,23,25–30] (for studies with a different number of colors or fermionic representation, see [20,21,24,31–49]). Therefore the authors encourage different groups to publish analogous studies, in order to fill this gap.

Some phenomenological results for the simulations presented in this work have already been published in a short paper [50] (see also [51,52]). A more detailed discussion of these results is currently in preparation.

II. WILSON FERMIONS IN A GENERIC REPRESENTATION

In four-dimensional Euclidean space the massless Wilson-Dirac operator is written following the notation in Ref. [53]:

$$D = \frac{1}{2}\sum_{\mu}[\gamma_\mu(\nabla_\mu + \nabla^*_\mu) - a\nabla^*_\mu\nabla_\mu], \tag{1}$$

where ∇ and ∇^* indicate, respectively, the forward and backward covariant derivatives:

$$\nabla_\mu f(x) = \frac{1}{a}[U(x,\mu)f(x+\mu) - f(x)], \tag{2}$$

$$\nabla^*_\mu f(x) = \frac{1}{a}[f(x) - U(x-\mu,\mu)^\dagger f(x-\mu)], \tag{3}$$

and $U(x,\mu)$ denote the link variables as usual. This expression is easily generalized to an arbitrary representation R of the gauge group; the action of the massive Dirac operator on a spinor field ψ yields

$$\begin{aligned} D_m\psi(x) &\equiv (D + m_0)\psi(x) \\ &= (4/a + m_0)\psi(x) - \frac{1}{2a}\sum_{\mu}\{(1-\gamma_\mu)U^R(x,\mu) \\ &\quad \times \psi(x+\mu) + (1+\gamma_\mu)U^R(x-\mu,\mu)^\dagger \\ &\quad \times \psi(x-\mu)\}, \end{aligned} \tag{4}$$

where U^R are the link variables in the representation R, and m_0 is the bare mass.

Let T^a_F and T^a_R be, respectively, the generators in the fundamental representation and in a generic representation R. Our conventions for the normalization of generators and other group—theoretical factors can be found in Appendix A. The explicit form of the generators used in this work is given in Appendix B. If the link variables in the fundamental representation are written as

$$U(x,\mu) = \exp[i\omega^a(x,\mu)T^a_F], \tag{5}$$

then the link variables in the representation R are given by

$$U^R(x,\mu) = \exp[i\omega^a(x,\mu)T^a_R], \tag{6}$$

where the functions $\omega^a(x,\mu)$ are *the same* in both equations. The explicit relation between link variables in different representations can be worked out explicitly for each individual case (see Appendix B). For instance, for the adjoint representation of SU(N) we have the well-known formula:

$$U^{\mathrm{adj}}_{a,b} = \tfrac{1}{2}\mathrm{tr}[T^a_F U T^b_F U^\dagger]. \tag{7}$$

The fermionic lattice action

$$S_f = a^4 \sum_x \bar{\psi}(x) D_m \psi(x) \tag{8}$$

is quadratic in the fermionic fields, and therefore its contribution to the partition function can be computed exactly, yielding the fermionic determinant, $\det D_m$. In numerical simulations, the latter determinant is conveniently replaced by the determinant of the Hermitian Dirac operator Q_m, defined as usual as

$$Q_m = \gamma_5 D_m. \tag{9}$$

The fermionic determinant for an even number n_f of degenerate flavors can be represented by introducing complex pseudofermionic (bosonic) fields ϕ, $\phi^\dagger$:

$$(\det D_m)^{n_f} = (\det Q_m)^{n_f} = \int \mathcal{D}\phi \mathcal{D}\phi^\dagger e^{-S_f}, \tag{10}$$

where the pseudofermionic action has the generic form

$$S_f = a^4 \sum_x \phi^\dagger(x)(Q_m^2)^{-l}\phi(x), \qquad l = n_f/2. \tag{11}$$

Note that we have used the same symbol S_f to denote the fermionic action written in terms of the usual Grassmann variables and the pseudofermionic action written in terms of bosonic fields that is used in the numerical simulations; the meaning of the symbol will be specified by the context in which it is used. In the above expression the square of Q_m is used and not the matrix itself because Q_m may not be positive definite. The sum over spin and color indices in the above formulas has been omitted in order to simplify the notation.

For the gauge action we always use the Wilson action written in terms of elementary 1×1 plaquettes built of link variables *in the fundamental representation*:

$$S_g = \beta \sum_{\mu<\nu} \left(1 - \frac{1}{N} \mathrm{Re}\,\mathrm{tr}\mathcal{P}_{\mu\nu}\right), \tag{12}$$

where $\beta = 2N/g_0^2$ is the lattice bare coupling. The algorithm can be generalized to other gauge actions without any major difficulty.

The partition function for the theory with n_f flavors of dynamical quarks can therefore be written as

$$Z = \int \mathcal{D}U \mathcal{D}\phi \mathcal{D}\phi^\dagger e^{-S_g(U) - S_f(U,\phi,\phi^\dagger)}. \tag{13}$$

It is also possible to work exclusively with link variables in the higher representation R, by writing the gauge action as a function of the latter. We expect the two choices to yield the same physics in the continuum limit, while a different phase structure may appear at strong coupling. We will not investigate this option here.

III. SIMULATION ALGORITHM

Simulations for this work are performed using the RHMC algorithm [54]. This is an exact algorithm which is flexible enough to cover all the cases of interest with good performances, while still maintaining a relatively simple form. The algorithm itself is a variation of the HMC algorithm [55] where rational approximations are used to compute fractional powers of the fermionic matrix Q_m^2 appearing for a generic number of flavors and pseudofermions. Both the HMC and RHMC set up a Markov chain of gauge field configurations yielding the desired limiting distribution using the same steps. The outline of the algorithms can be summarized as follows: (i) generate new pseudofermion fields from a heat bath; (ii) evolve the gauge field configuration following the flow of a fictitious Hamiltonian with randomly chosen initial momenta for each link variable—this step is usually called molecular dynamic (MD) evolution; (iii) perform a Metropolis test at the MD trajectory to correct for errors in the integration of the equation of motion at the previous step.

Our implementation of the HMC/RHMC is a straightforward adaptation of the standard technique to the case under consideration. As usual the bottleneck of the algorithm is the inversion of the Dirac operator Q_m^2 that is needed during the MD evolution. To reduce the number of steps in the integration of the equation of motion and thus the number of inversions, we use the second order Omelyan integrator [56] for the MD evolution with different time steps for the gauge and fermion action. Multiple pseudofermions and the even-odd preconditioning of the fermionic determinant are also used in this paper, but no other acceleration techniques are necessary for the purpose of this work. More extensive simulations will require a more careful study of these issues.

In the rest of this section we will describe the modifications required to handle fermions in a generic representation and the implementation details used in our code.

A. HMC molecular dynamics

In the following the expression for the force needed in the molecular dynamics is generalized to the case of fermions in a generic representation. Since simulations in arbitrary representations are still at their early stages, we decide to derive the forces in detail, in order to define the quantities that appear in the simulations as clearly as possible. Introducing for each link variable a conjugate momentum in the algebra of the gauge group:

$$\pi(x,\mu) = i\pi^a(x,\mu)T^a_F, \tag{14}$$

a fictitious Hamiltonian H is written on the group manifold as

$$H = H_\pi + H_g + H_f, \tag{15}$$

where, assuming $n_f = 2$,

$$H_\pi = \frac{1}{2}\sum_{x,\mu}(\pi(x,\mu),\pi(x,\mu)) = \frac{1}{2}T_F\sum_{a,x,\mu}\pi^a(x,\mu)^2, \quad (16)$$

$$H_g = S_g = \beta\sum_{\mu<\nu}\left(1-\frac{1}{N}\,\mathrm{Re\,tr}\mathcal{P}_{\mu\nu}\right), \quad (17)$$

$$H_f = S_f = \sum_x \phi^\dagger(x)[Q_m^2 - s]^{-1}\phi(x). \quad (18)$$

Since the momenta are conjugate to the link variables, they are defined in the fundamental representation.

The cases where $n_f \neq 2$ are dealt using the RHMC algorithm described in the next section. Also note that an arbitrary shift s has been included in the fermionic action which will be useful for the discussion of the RHMC algorithm.

Denoting by τ the fictitious time of this Hamiltonian system, the equations of motion are given by

$$\frac{d}{d\tau}U(x,\mu) = \pi(x,\mu)U(x,\mu), \quad (19)$$

$$\frac{d}{d\tau}\pi(x,\mu) = F(x,\mu), \quad (20)$$

where the right-hand side of the second equation above defines the force $F(x,\mu)$ that drives the time evolution of the momenta.

For a generic infinitesimal variation of a link variable,

$$\delta U(x,\mu) = \delta\omega(x,\mu)U(x,\mu), \quad (21)$$

where $\delta\omega(x,\mu) = i\delta\omega^a(x,\mu)T_F^a$ is an element of the algebra, $F(x,\mu)$ is obtained from the corresponding variation of the action through the equations

$$F(x,\mu) = F_g(x,\mu) + F_f(x,\mu), \qquad \delta S_g = -(\delta\omega, F_g),$$
$$\delta S_f = -(\delta\omega, F_f).$$

Since we use link variables in the fundamental representation for the gauge action S_g, the variation of the latter is the usual one that appears in the HMC molecular dynamics evolution:

$$\delta S_g = -\frac{\beta}{N}\sum_{x,\mu,a}\delta\omega^a(x,\mu)\,\mathrm{Re\,tr}[iT_F^a U(x,\mu)V^\dagger(x,\mu)], \quad (22)$$

where $V(x,\mu)$ is the sum of the forward and backward staples around the link $U(x,\mu)$.

The fermionic force is obtained from the variation of the fermionic action as follows. Starting from

$$\delta S_f = -\phi^\dagger(Q_m^2 - s)^{-1}\delta(Q_m^2)(Q_m^2 - s)^{-1}\phi, \quad (23)$$

let us define

$$\eta = (Q_m^2 - s)^{-1}\phi, \quad (24)$$

$$\xi = Q_m\eta; \quad (25)$$

using the fact that the matrix $(Q_m^2 - s)$ is Hermitian, we can rewrite Eq. (23) as

$$\delta S_f = -2\,\mathrm{Re}[\xi^\dagger\delta(Q_m)\eta]. \quad (26)$$

Inserting the explicit form of Q_m, Eq. (9), into Eq. (26), we obtain

$$\delta S_f = \mathrm{Re}\sum_{x,\mu}[\xi(x)^\dagger\delta U^R(x,\mu)\gamma_5(1-\gamma_\mu)\eta(x+\mu) + \eta(x)^\dagger\delta U^R(x,\mu)\gamma_5(1-\gamma_\mu)\xi(x+\mu)], \quad (27)$$

where we are implicitly summing over spin and color indices. We can now write the variation of U^R as

$$\delta U^R(x,\mu) = \delta\omega^R(x,\mu)U^R(x,\mu) = i\delta\omega^a(x,\mu)T_R^a U^R(x,\mu), \quad (28)$$

where the $\delta\omega^a(x,\mu)$ in the above equation are the same functions that define the variation of the gauge link in Eq. (21). Equation (27) and (28) yield

$$\delta S_f = \sum_{x,\mu,a}\delta\omega^a(x,\mu)\,\mathrm{Re\,tr}_{c,s}[iT_R^a U^R(x,\mu)\gamma_5(1-\gamma_\mu) \times\{\eta(x+\mu)\otimes\xi(x)^\dagger + \xi(x+\mu)\otimes\eta(x)^\dagger\}]. \quad (29)$$

Here the symbol $\mathrm{tr}_{c,s}$ indicates the trace over color and spin.

For the sake of convenience we introduce the following projectors P_R^a over the algebra in the representation R:

$$P_R^a(F) = -\frac{1}{T_F}\,\mathrm{Re\,tr}_c[iT_R^a F], \quad (30)$$

and the following trace operator:

$$\mathrm{Tr}_{x,\mu}(\eta,\xi) = \mathrm{tr}_s[\gamma_5(1-\gamma_\mu)\{\eta(x+\mu)\otimes\xi(x)^\dagger + \xi(x+\mu)\otimes\eta(x)^\dagger\}]. \quad (31)$$

The forces are then given by

$$F_G^a(x,\mu) = -\frac{\beta}{N}P_F^a(U(x,\mu)V^\dagger(x,\mu)), \quad (32)$$

$$F_F^a(x,\mu) = P_R^a(U^R(x,\mu)\,\mathrm{Tr}_{x,\mu}(\eta,\xi)). \quad (33)$$

Note that when R is chosen to be the fundamental representation, the usual expressions for the fermionic force are recovered. Explicit expressions for the forces had already been computed for the case of fermions in the adjoint representation of the gauge group SU(2) in Ref. [57]. As an analytic check, we have verified that our result above agrees with Eq. (16) in Ref. [57].

B. RHMC implementation

The fermionic part of the HMC Hamiltonian, for n_f degenerate fermions and N_{pf} pseudofermions, can be written as

$$H_f = \sum_{k=1}^{N_{pf}} \phi_k^\dagger (Q_m^2)^{-l_k} \phi_k; \qquad \sum_{k=1}^{N_{pf}} l_k = \frac{n_f}{2}. \tag{34}$$

For the sake of simplicity we will set all the l_k to be equal:

$$\forall k, \qquad l_k = \frac{n_f}{2N_{pf}}. \tag{35}$$

The above decomposition is used in the RHMC algorithm [54], where rational approximations are used to compute the fractional powers of the positive definite fermion matrix Q_m^2. Even though we will work at fixed $n_f = 2$ in this paper, the RHMC is particularly useful if one wants an algorithm that can easily be generalized to an arbitrary number of fermions. Three different rational approximations are used for this implementation.

The first rational approximation is required in the heat-bath update of pseudofermions. In order to generate pseudofermions distributed as in Eq. (34), a simple two-step process is used. For each pseudofermion we first generate a Gaussian distributed field $\tilde{\phi}_k$ with probability

$$P(\tilde{\phi}_k) \propto \exp[-\tilde{\phi}_k^\dagger \tilde{\phi}_k], \tag{36}$$

and then we set

$$\phi_k = (Q_m^2)^{(l_k/2)} \tilde{\phi}_k, \tag{37}$$

making use of the fact that (Q_m^2) is Hermitian (notice the plus sign in the exponent). The RHMC algorithm uses a rational approximation to compute the above quantities (we need only one approximation since all l_k are equal):

$$r_a(Q_m^2) = \alpha_0^a + \sum_{n=1}^{d_1} \alpha_n^a (Q_m^2 - s_n^a)^{-1} \simeq (Q_m^2)^{(l_k/2)}. \tag{38}$$

The second rational approximation is used to approximate Eq. (34) during the molecular dynamics evolution (as before only one approximation is needed because all l_k are equal):

$$H_F = \sum_{k=1}^{N_{pf}} \phi_k^\dagger r_b(Q_m^2) \phi_k, \tag{39}$$

$$r_b(Q_m^2) = \alpha_0^b + \sum_{n=1}^{d_2} \alpha_n^b (Q_m^2 - s_n^b)^{-1} \simeq (Q_m^2)^{-l_k}. \tag{40}$$

Using the formulas derived in Sec. III A, it is easy to write the force corresponding to Eq. (39). In fact, Eq. (39) is nothing but a sum of terms of the form Eq. (18) once we put $l = 1$, $s = s_n^b$. The RHMC force will then be given by a sum over $n = 1, \ldots, d_2$ of terms given by Eq. (33) multiplied by a factor α_n^b. It is possible to compute all the η's defined in Eq. (24) corresponding to different s_n^b simultaneously with a multishift inverter.

The third rational approximation is used for the Metropolis test. Starting from Eq. (34), for each pseudofermion we can rewrite

$$\phi_k^\dagger (Q_m^2)^{-l_k} \phi_k = \|(Q_m^2)^{-(l_k/2)} \phi_k\|^2, \tag{41}$$

where we used the property that Q_m^2 is Hermitian. The rational approximation needed in this case is

$$r_c(Q_m^2) = \alpha_0^c + \sum_{n=1}^{d_3} \alpha_n^c (Q_m^2 - s_n^c)^{-1} \simeq (Q_m^2)^{-(l_k/2)}. \tag{42}$$

Notice that if $d_1 = d_3$, the coefficients for the two approximations r_a and r_c can each be obtained from the other.

The coefficients α_n, s_n appearing in the rational approximations are computed using the Remez algorithm. In this implementation we do not compute the coefficients "on the fly," but instead the required values are taken from a look-up table that has been precomputed, according to the following prescription.

First note that we need to compute rational approximations for a function $f(x)$ of the form $f(x) = x^l$ and the approximation must be accurate over the spectral range of the operator Q_m^2. To simplify the computation of the table we note that the following proposition holds: if $f(x)$ is a homogeneous function of degree l and $r(x)$ is an optimal (in the sense of relative error) rational approximation to $f(x)$ over the interval $[\epsilon, \mathrm{h}]$ to a given accuracy, then $r(kx)/k^l$ is an optimal rational approximation for the same function and the same accuracy over the interval $[\epsilon/k, \mathrm{h}/k]$. Moreover the coefficients of this "rescaled" rational approximation are easily obtained from that of the original approximation. A simple corollary is that we can divide the optimal rational approximations of a given homogeneous function $f(x)$ with the same relative precision, in classes labeled by the ratio ϵ/h. Within each of these classes the coefficients of the rational approximations are easily related to each other, so that we only need to compute one rational approximation in each class. Thus all that is needed in practice is a table containing the coefficients of rational approximations for each of these classes, for each function $f(x)$ which we want to approximate and for each relative precision which is required. At run-time this table is used to generate optimal rational approximations rescaling the precomputed coefficients to the desired interval containing the spectrum of the matrix Q_m^2. This interval is obtained by computing the maximum and minimum eigenvalue of Q_m^2 on each configuration when needed.

C. Even-odd preconditioning

As already pointed out above, the time required for the inversions of the Dirac operator is one of the dominant contributions to the total cost of the simulation. The con-

vergence of such inversions can be improved using an appropriate preconditioning. The idea behind preconditioning is to rewrite the fermionic determinant as a determinant (or product of determinants) of one (or more) better conditioned matrix (matrices) than the original Dirac operator. Very effective preconditionings are at the heart of the recent progress in simulations of QCD with dynamical fermions. For the scope of this work, we use a simple *even-odd* preconditioning [58]. We review the main features of even-odd preconditioning here in order to explain the modifications that are required when considering higher-dimensional representations. We divide the lattice in a sublattice of even points Λ_e and another sublattice of odd points Λ_o, and we rewrite the Dirac operator D_m as a block matrix:

$$D_m = \begin{pmatrix} 4+m & D_{eo} \\ D_{oe} & 4+m \end{pmatrix}, \tag{43}$$

where each block has a dimension half that of the original Dirac matrix. The diagonal blocks connecting sites with the same parity are proportional to the identity matrix, while off-diagonal blocks connect sites with opposite parity. We have (since D_m is γ_5 Hermitian)

$$\gamma_5 D_{eo} \gamma_5 = D_{oe}^\dagger. \tag{44}$$

The determinant of the Dirac matrix D_m can be rewritten as

$$\det D_m = \det[(4+m)^2 - D_{eo}D_{oe}] \equiv \det D_m^{eo}, \tag{45}$$

using the well-known expression for the determinant of a block matrix. Since the determinant of D_m and of D_m^{eo} are the same, the latter can be used in numerical simulations. Note that the even-odd preconditioned matrix only connects sites with the same parity; thus it has only half of the size of the original Dirac matrix and, like D_m, it is γ_5Hermitian. We define as before the Hermitian matrix $Q_m^{eo} \equiv \gamma_5 D_m^{eo}$, which will be used in practice.

The formulation of the HMC algorithm does not change and the only difference is that pseudofermion fields are now defined on only half of the lattice sites, conventionally the even sites in what follows. We now derive the explicit expression for the fermionic force for the preconditioned system described by the Hamiltonian:

$$H_f = \phi_e^\dagger [(Q_m^{eo})^2 - s]^{-1} \phi_e, \tag{46}$$

where as before we are assuming $n_f = 2$ or a rational approximation of the actual fractional power function; the suffix in ϕ_e is an explicit reminder that the pseudofermion field is defined on only even sites. Equation (26) is unchanged :

$$\delta S_f = -2\,\mathrm{Re}[\xi_e^\dagger \delta(Q_m^{eo}) \eta_e], \tag{47}$$

where as before we have defined

$$\eta_e = ((Q_m^{eo})^2 - s)^{-1} \phi_e, \tag{48}$$

$$\xi_e = Q_m^{eo} \eta_e. \tag{49}$$

The explicit form of Q_m^{eo} must be used at this point. We have

$$\delta(Q_m^{eo}) = -\gamma_5(\delta D_{eo} D_{oe} + D_{eo}\delta D_{oe}). \tag{50}$$

Defining

$$\eta_o = D_{oe}\eta_e, \tag{51}$$

$$\xi_o = D_{oe}\xi_e, \tag{52}$$

and inserting Eq. (50) into Eq. (47), we arrive at the same expression as before for the variation of the action, but with a minus sign:

$$\delta S_F = -\sum_{\mu,x} \mathrm{Re}\,\mathrm{tr}_c[\delta U^R(x,\mu)\,\mathrm{Tr}_{x,\mu}(\eta,\xi)]. \tag{53}$$

From Eq. (53) and proceeding as before we arrive at the final expression for the force. This again coincides with Eq. (33) but with the opposite sign:

$$F_F^a(x,\mu) = -P_R^a(U^R(x,\mu)\,\mathrm{Tr}_{x,\mu}(\eta,\xi)). \tag{54}$$

D. Some details on the implementation

As the algorithm is implemented for the first time, we describe in this section some general features of our code and the technical solutions adopted to manage fermion fields defined in an arbitrary representation.

At this early stage in our physics studies we prioritize the flexibility of the code over the optimization aspects. The code is written in ANSI C for maximum portability to different architectures. This choice is justified, in our opinion, by the fact that, on this relatively small scale, C codes maintain a much higher overall simplicity and clarity compared to e.g. C++ codes with a comparable low overhead.

The major difference with respect to conventional codes—i.e. codes for simulations of the SU(3) gauge group with fundamental fermions—is obviously that all operations involving gauge links or pseudofermion fields must be able to handle matrices and vectors of arbitrary dimension. In the generic case of four-dimensional SU(N) with fermions in a representation R, link matrices for the gauge action have dimension $N \times N$, the represented gauge links have dimension $d_R \times d_R$, and fermion fields have dimension $4d_R$. These numbers indicate how the cost of the simulation scales both in memory and in the number of floating point operations per application of the Dirac operator as N and R are varied. One simple way to handle these objects would be to have functions that implement operations on them, taking as an additional parameter the dimensions of the objects themselves. However, we found it more flexible to use the following approach. We use preprocessor macros instead of functions.[1] We fix the

[1]Inline functions could work just as well; however, the handling of inlining is a feature which depends on the compiler.

gauge group and the representation R at compile time as this gives the opportunity to more optimizations (e.g. partial unrolling of loops).[2] All of the required macros are automatically generated in a precompiling step. We use a simple Perl program for this purpose whose input parameters are the number of colors N and the representation R and whose output is a C header file containing the macro functions. The whole process of header generation and compilation is managed through a custom Makefile system, and it is thus completely transparent to the end user.

A second difference with respect to conventional codes is that it is convenient, although not strictly necessary, to have a second copy of the gauge field in the representation R. This is only used in the computation of the fermionic force [see Eq. (33)], and it is also useful to impose boundary conditions on the fermion fields. Every time the gauge field is updated during the molecular dynamics evolution, the represented gauge field needs to be recomputed.

At this early stage of simulations, we chose to use double precision everywhere in the code to reduce the risk of problems arising from numerical accuracy. This is done at the expense of optimal performance, which we feel is justified in this study of the algorithm implementation and behavior. As the source of random numbers, we use the RANLUX generator [59].

IV. BEHAVIOR OF THE ALGORITHM

In this section we shall discuss some simple tests of the RHMC algorithm with the aim to show the correctness of our implementation. The majority of the tests performed for this purpose were run on the lattice T2-B11 (see Table I below) which corresponds to our biggest volume and the lightest mass at $\beta = 2$. For all the tests in this section we have used even-odd preconditioning and two pseudofermion fields.

A. Preliminary tests

A simple test of the algorithm is to look at the expectation value $\langle \exp(-\Delta H) \rangle$, where ΔH is the difference of the values of the Hamiltonian H at the beginning and at the end of a trajectory in the molecular dynamics evolution. This expectation value should always be 1 (a result known as Creutz equality [60]). Moreover since the RHMC is an exact algorithm, i.e. there are no corrections due to the errors occurring in the molecular dynamics integration, a good test of the algorithm is to check whether or not there is any dependence of any quantity on the integration step size $\Delta\tau$. The average plaquette $\langle P \rangle$ is a good candidate for this purpose because it can be measured with high accuracy.

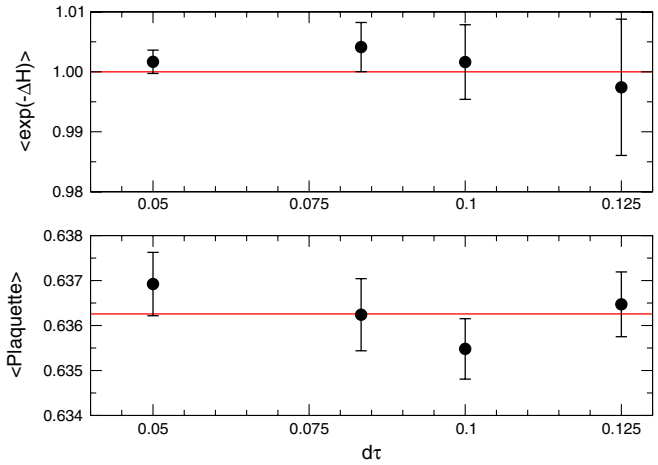

FIG. 1 (color online). Dependence of $\langle \exp(\Delta H) \rangle$ and $\langle P \rangle$ on the time step used for the MD integration.

We show in Fig. 1 the quantities $\langle \exp(-\Delta H) \rangle$ (upper panel) and the average plaquette (lower panel) for four different step sizes of the MD integration. No statistically significant deviations from the expected behavior are seen. The value of $\langle P \rangle$ is consistently independent on $\Delta\tau$ and the Creutz's equality $\langle \exp(-\Delta H) \rangle = 1$ is satisfied. Notice also that for the latter quantity the error bars become smaller as $\Delta\tau$ goes to zero, as expected from the fact that $\langle \Delta H \rangle$ is also vanishing in the same limit. This is explicitly shown in the upper panel of Fig. 2. As expected for a second order integrator (see [61]), the quantity $\langle \Delta H \rangle$ is proportional to $\Delta\tau^4$ with very good accuracy (the red curve in the plot is

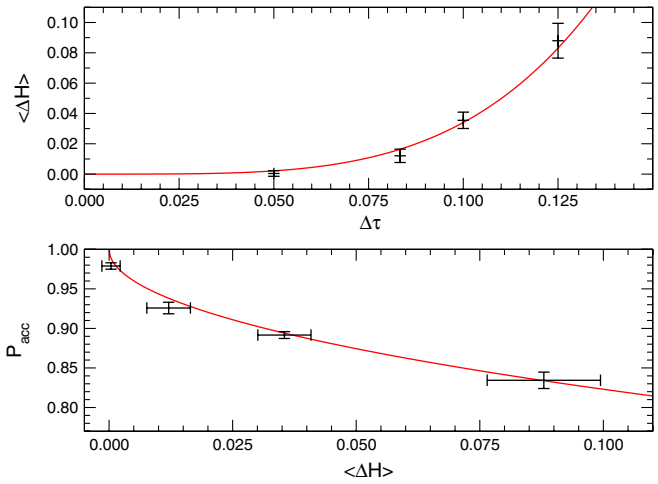

FIG. 2 (color online). The expectation value $\langle \Delta H \rangle$ is proportional to $(\Delta\tau)^4$ (upper panel) consistently with the use of a second order integrator (the red curve shows the one parameter fit). The acceptance probability P_{acc} as measured in the test runs (lower panel) is correctly described by the expected large volume behavior $P_{\text{acc}} = \text{erfc}(\sqrt{\langle \Delta H \rangle}/2)$ (solid curve, not a fit).

[2]This also means that recompiling is needed whenever the number of colors or the fermions' representation is changed. However, since the total compilation time, including the automatic generations of the required header, is less than one minute and independent on N, this can hardly be a problem.

the best fit to that functional form with one free parameter). The acceptance probability $P_{\rm acc}$ can also be used as a test of the correctness of the algorithm. In fact, in the large volume limit this probability is given by $P_{\rm acc} = \mathrm{erfc}(\sqrt{\langle \Delta H \rangle}/2)$ [62]. We show the measured value of the acceptance rate as a function of the average Hamiltonian variation in the lower panel of Fig. 2. The same figure shows also the predicted behavior (solid curve). We found a convincing agreement with the expectations.

As a last test in this section we measured reversibility violations in the MD. We remind the reader that this is a necessary condition for the correctness of the algorithm. The discussion will follow that of Ref. [63]. At the ''microscopic'' level, reversibility violations can occur when updating the gauge variables and in the momenta update during the MD evolution. We deal with the first source of nonreversibility using the trick suggested in Ref. [3]: the link update Eq. (19) is implemented by left multiplication of an exactly unitary matrix $E[\pi(x,\mu)]$ such that $E[\pi(x,\mu)]E[-\pi(x,\mu)] = 1$ and which is also an approximation to the exponential map. In this way no possible reversibility violations can arise (within machine precision) in the link update. For the momenta update, local reversibility is guaranteed by the use of double precision and the requirement of a small relative residue (10^{-7} in our simulations) for the force calculation. The solution of the linear system required for the force calculation itself is always started from the same trial solution. At the ''global'' level we measured the reversibility violations through the quantity $|\delta H|$ defined as the average difference between the Hamiltonian of the starting configuration and the one obtained evolving the system forward for a unit of Monte Carlo time and then back (flipping the momenta at $\tau = 1$) to the original position in phase space. This measure of reversibility violations is shown in Fig. 3. The global violations to reversibility appear to be very small and independent on $\Delta\tau$ and hence also on $\langle \Delta H \rangle$.

B. Checks for SU(3) with $n_f = 2$ in the fundamental representation

The routines that perform linear algebra operations in color space for arbitrary representations are generated automatically by a Perl program. As a first nontrivial test of our implementation, our code should correctly reproduce the results for simulations in the fundamental representation of SU(3). The code has been benchmarked for SU(3) with $n_f = 2$ against simulations obtained using the domain decomposition (DD)–HMC algorithm [3] on small lattices. Figure 4 shows the thermalization of the plaquette at $\beta = 6.0$. On small lattices, the DD-HMC only updates a small fraction of the links in the system, and therefore the thermalization is much slower in units of MC trajectories. To compare the two time histories we have therefore rescaled the trajectory number for the DD-HMC data. The figure shows a very good agreement between the two simulations, in particular, for the equilibrium value of the plaquette.

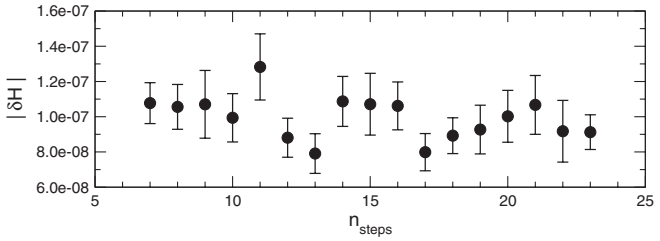

FIG. 3. Reversibility test for several values of the time step used for the MD integration.

Another test of the algorithm is obtained by simulating the SU(3) theory with two flavors in the fundamental representation and in the two-index antisymmetric one. For the theory with three colors the two representations are equivalent and related by charge conjugation. We have compared the outcomes of two simulations on $4^3 \times 8$ lattice at $\beta = 5.6$ and $\kappa = 0.15600$. The time-history of the plaquette and its probability distribution for the two simulations are summarized in Fig. 5. Once again we find a very convincing agreement between the two simulations.

C. SU(2) $n_f = 2$ two-index symmetric

The theory with two colors and two Dirac fermions in the two-index symmetric ($2S$) representation has been proposed as a phenomenologically relevant candidate for a minimal walking technicolor theory. For the specific case of the SU(2) color group, the $2S$ representation is equivalent to the adjoint representation and is therefore real, which makes it less intensive from the computational point of view. Analytical results for the Λ parameter, the renormalization constant, and the possibility of an Aoki phase at

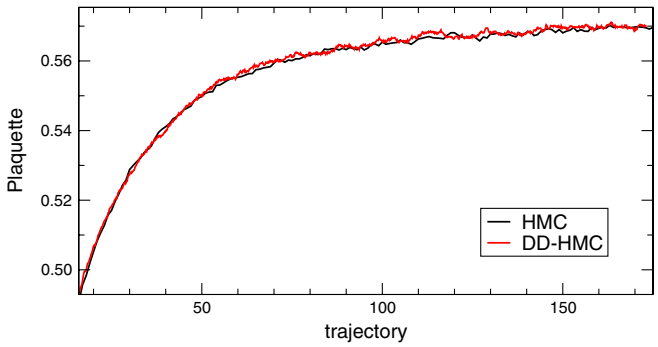

FIG. 4 (color online). Time history for the thermalization of the plaquette in the SU(3) theory with two flavors in the fundamental representation on a 16^4 lattice at $\beta = 5.6$ and $\kappa = 0.157\,50$. The black line shows the evolution of the plaquette value using our HMC algorithm, while the red line represents the same quantity using the DD-HMC algorithm. Trajectory number has been scaled by a factor of 7 for the DD-HMC data.

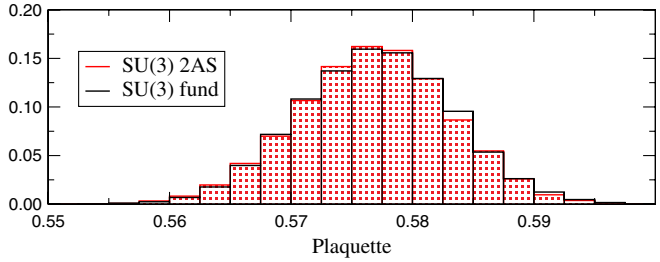

FIG. 5 (color online). Probability distribution of the plaquette. The black (respectively, red filled) curve refers to data from a simulation of the SU(3) gauge theory on a $4^3 \times 8$ lattice at $\beta = 5.6$, $\kappa = 0.156\,00$ with two fermions in the fundamental representation (respectively, the two-index antisymmetric).

finite lattice spacing have been presented in Ref. [64], where the theory was denoted T2. We will adopt the same conventions here. Preliminary results from lattice simulations of this theory were presented in Ref. [25]. In this subsection we build upon this previous experience and provide some more extensive descriptions of the behavior of numerical simulations in the space of bare parameters. The list of runs is summarized in Table I for inverse coupling $\beta = 2.0$ and in Table II for inverse coupling $\beta = 2.25$.

This theory allows us to perform a nontrivial check of our code generation. The link variables in the higher representation can be built in two different manners: in one case we construct real matrices according to Eq. (7), while in the other case we use our generic algorithm for constructing the $2S$ complex representation of SU(N), as described in Appendix B. As expected, for a given configuration in the fundamental representation the two representations yield exactly the same matrices; the generic algorithm produces complex 3×3 matrices with vanishing imaginary parts. Evolving the configuration using the HMC with the two different representations yields compatible results as one can see by the comparison of the runs T2-A1 and T2-A1′ shown in Fig. 6 for the case of the plaquette.

TABLE I. List of runs for the $T2$ theory at inverse coupling $\beta = 2.0$. The standard runs are performed using link variables in the real adjoint representation. The primed run is performed with link variables in the $2S$ representation that are constructed in an algorithmic way as complex 3×3 matrices. In order to simplify the comparison with the runs in Ref. [25] we list both the values of κ and m.

Lattice	V	κ	$-am_0$	N_{traj}	$\langle P \rangle$	τ
T2-A1	8×4^3	0.125 00	0.0	28 800	0.5093(14)	2.9(0.4)
T2-A2	8×4^3	0.142 86	0.5	28 800	0.5163(16)	3.1(0.5)
T2-A3	8×4^3	0.153 85	0.75	28 800	0.5235(18)	3.1(0.5)
T2-A4	8×4^3	0.166 67	1.0	28 800	0.5373(20)	6.0(1.2)
T2-A5	8×4^3	0.181 82	1.25	27 200	0.5742(37)	12.0(3.6)
T2-A6	8×4^3	0.183 82	1.28	25 600	0.5850(50)	22.3(9.3)
T2-A7	8×4^3	0.185 87	1.31	41 600	0.6013(55)	48.3(23.3)
T2-A8	8×4^3	0.186 57	1.32	51 200	0.6159(58)	40.7(16.3)
T2-A1′	8×4^3	0.125 00	0.0	3000	0.5094(45)	2.7(1.2)
T2-B7	16×8^3	0.185 87	1.31	3200	0.5951(42)	5.8(3.6)
T2-B8	16×8^3	0.186 57	1.32	1600	0.6040(56)	9.0(9.6)
T2-B9	16×8^3	0.186 92	1.325	2240	0.6107(53)	4.2(2.6)
T2-B10	16×8^3	0.187 27	1.33	1100	0.6168(73)	2.6(1.8)
T2-B11	16×8^3	0.187 97	1.34	3840	0.6347(58)	13.6(11.5)

The critical value of the hopping parameter has been computed in perturbation theory in Ref. [64], to which we refer the reader for the notation and results used in what follows. Using the cactus resummed formula for the theory under consideration, we find

$$m_c = g_0^2 2C_2(R) \times (-0.162\,857)/\tilde{c}_0, \tag{55}$$

where $\tilde{c}_0$ is a function of g_0 defined by solving the following equation:

$$\tilde{c}_0 = e^{-g_0^2/(16\tilde{c}_0)}\left(1 - \frac{g_0^2}{24\tilde{c}_0}\right). \tag{56}$$

For $\beta = 2.0$ and $\beta = 2.25$ the above formula yields, respectively, $m_c = -1.73$ ($\kappa_c = 0.220$) and $m_c = -1.47$ ($\kappa_c = 0.198$). A nonperturbative determination of the chiral limit in the space of bare parameters (β, κ) can be obtained by linear extrapolation of the partially conserved axial current (PCAC) mass, or of the mass squared of the pseudoscalar Goldstone boson. Because of the power divergencies in the renormalization of the bare quark mass, any perturbative computation of m_c is expected to receive nonperturbative corrections $\mathcal{O}(e^{-1/g_0^2(a)}/a)$. Therefore the perturbative computation can at best yield an indication of the location of the critical point. The detailed study of these quantities is presented in the next section.

In order to check that the range of κ values does not lead to exceptionally small values of the eigenvalues of the Dirac operator, we have monitored the distribution of the smallest eigenvalue of Q_m^{eo} following the study in Ref. [4]. The histograms that describe the distribution of the lowest eigenvalue of $|Q_m^{eo}|$ are displayed in Fig. 7 for the simulations at $\beta = 2.25$. At the values of κ that we have considered, the spectrum of the Dirac operator has a clear gap. This is reflected in a smooth behavior of the simulations even at the lightest masses, as can be seen in the time histories for the plaquette and the solver number reported in Fig. 8. The results obtained with fundamental fermions in Ref. [4] suggest that the width of the distribution scales like $a/\sqrt{V}$ as the continuum and thermodynamic limits are approached. A comparison of the standard deviations of the eigenvalue distributions for the simulations at $\beta = 2.25$ shows that this scaling is well verified for the theory under consideration (Fig. 9).

As a final test of the algorithm we monitored the MC integration forces for the RHMC algorithm. Compatibly with the absence of exceptionally small eigenvalues, these forces appear to behave smoothly as a function of the bare

TABLE II. List of runs for the $T2$ theory at inverse coupling $\beta = 2.25$. In the last two columns we give the average of the smallest eigenvalue of $|Q_m^{eo}|$ and its integrated autocorrelation time.

Lattice	V	$-am_0$	N_{traj}	$\langle P \rangle$	τ	λ	τ_λ
T2-C0	16×8^3	0.95	7601	0.635 77(16)	5.45(72)	3.582(13)	8.6(1.4)
T2-C1	16×8^3	0.975	7701	0.638 43(15)	5.43(71)	2.982(12)	6.65(96)
T2-C2	16×8^3	1	7801	0.641 36(15)	5.10(64)	2.427(11)	6.28(88)
T2-C3	16×8^3	1.025	7801	0.644 63(15)	4.29(50)	1.894(10)	6.07(84)
T2-C4	16×8^3	1.05	7801	0.647 93(15)	3.48(36)	1.4596(79)	4.39(52)
T2-C5	16×8^3	1.075	6400	0.651 79(16)	2.99(32)	1.0692(74)	4.27(55)
T2-C6	16×8^3	1.1	6400	0.655 66(16)	3.28(37)	0.7564(60)	3.77(45)
T2-C7	16×8^3	1.125	7073	0.660 37(15)	2.99(30)	0.4854(43)	3.03(31)
T2-C8	16×8^3	1.15	6400	0.665 50(16)	3.31(37)	0.2779(31)	2.80(29)
T2-C9	16×8^3	1.175	6400	0.671 77(17)	3.24(36)	0.1351(18)	2.80(29)
T2-D0	24×12^3	0.95	10 201	0.635 310(59)	6.16(74)	3.5058(50)	3.08(26)
T2-D1	24×12^3	1	8652	0.640 998(64)	4.92(58)	2.4218(44)	3.10(29)
T2-D2	24×12^3	1.05	7819	0.647 633(70)	6.79(99)	1.4936(51)	5.80(78)
T2-D3	24×12^3	1.075	7186	0.651 630(68)	4.61(58)	1.0553(40)	4.95(64)
T2-D4	24×12^3	1.1	6393	0.655 827(76)	4.09(51)	0.7202(30)	7.8(1.3)
T2-D5	24×12^3	1.125	6200	0.660 588(75)	3.97(50)	0.4419(22)	5.98(91)
T2-D6	24×12^3	1.15	1599	0.665 88(15)	3.71(90)	0.2271(31)	6.6(2.1)
T2-D7	24×12^3	1.175	5582	0.672 074(79)	4.22(58)	0.086 41(90)	3.78(49)
T2-D8	24×12^3	1.18	4081	0.673 474(92)	4.01(63)	0.065 61(92)	10(2.5)
T2-D9	24×12^3	1.185	4201	0.675 094(93)	3.42(49)	0.051 96(71)	3.53(51)
T2-D10	24×12^3	1.19	3501	0.676 63(10)	4.15(70)	0.039 85(61)	5.2(1.0)
T2-E0	32×16^3	1.15	5446	0.665 894(44)	3.32(40)	0.2227(10)	3.05(36)
T2-E1	32×16^3	1.175	2192	0.672 235(73)	2.80(50)	0.070 36(90)	5.9(1.5)
T2-E2	32×16^3	1.18	4606	0.673 657(49)	3.46(47)	0.051 67(50)	6.1(1.1)
T2-E3	32×16^3	1.185	4313	0.675 170(50)	2.99(39)	0.037 51(38)	4.66(75)
T2-E4	32×16^3	1.19	5404	0.676 637(44)	3.29(40)	0.024 74(28)	7.9(1.5)
T2-F0	64×24^3	1.18	458	0.673 737(46)	4.0(1.9)	0.044 36(51)	3.5(1.5)
T2-F1	64×24^3	1.185	291	0.675 184(59)	2.3(1.1)	0.028 36(59)	4.2(2.5)
T2-F2	64×24^3	1.19	349	0.676 649(52)	1.63(59)	0.015 20(39)	5.7(3.6)

mass and we observe a very mild (consistent with zero) dependence on the size of the lattice at constant am_0. In the upper panel of Fig. 10 we show the modulus of the force $|F_F^a(x, \mu)|$ averaged over all the lattice points x and all directions μ for each term of the rational approximation indexed by n. Data for two different volumes at the same value of the bare quark mass are shown corresponding to the lattices T2-E2 and T2-F0. The average fermionic force appears to change very little once the equilibrium is reached which is reflected in the plot by the fact that errors on this quantity are really small and not visible on the scale of the graph. The relative error for the average force ranges from a few per mille for $n = 1$ to less than 1% for $n = 11$. The variation with volume is also very small: the two average values appear to be always consistent with each other within errors. In the bottom panel of Fig. 10 we report for completeness the size of the rational approximation coefficients used in the simulation. Their variation is also quite small, given that the distribution of the smallest and largest eigenvalues of the Dirac operator is quite narrow as discussed above.

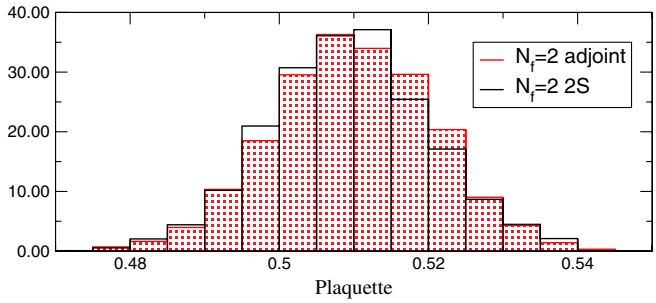

FIG. 6 (color online). Normalized histogram of the plaquette distribution. Data for the SU(2) theory with two flavors in the adjoint representation (red filled curve) are compared with data for two flavors in the two-index symmetric representation (black curve).

The dependence of the average fermionic forces on the bare quark mass is shown in Fig. 11 for the T2-F lattice. The change with the quark mass is quite small but visible in this case, and more pronounced for higher values of n, corresponding to smaller shifts.

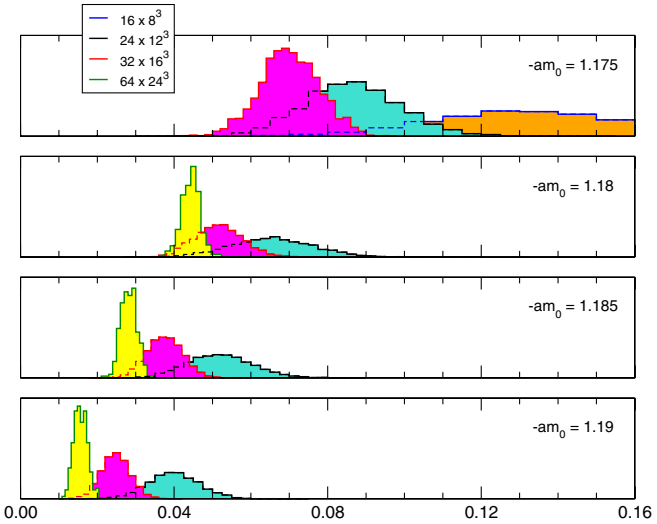

FIG. 7 (color online). Probability distribution of the lowest eigenvalue of the Dirac operator for $\beta = 2.25$.

D. Autocorrelation times

The integrated autocorrelation time for the plaquette during our runs is computed in units of molecular dynamics time following Ref. [65]. The results are reported in Table I, where an increase of the autocorrelation time is clearly visible as we move to lighter fermion masses. In all cases the autocorrelation time is short compared to the total length of the simulations, which guarantees that the binned configurations used for our analyses can be considered as independent and therefore the statistical error is correctly estimated from the variance of the ensembles. It is worthwhile to emphasize that extensive simulations of QCD have shown that the autocorrelation time depends on the trajectory length [66] and on the lattice spacing. Our runs are all performed with trajectories of unit length. Moreover a critical slowing down of the topological modes has been highlighted in the time histories of the topological charge [67]. Therefore we expect that the observables that are more strongly correlated with topology show a greater correlation length as we approach the continuum limit. These issues need to be kept in mind as the simulations evolve and more precise estimates of the phenomenological quantities will be sought. Finally, one should keep in mind that autocorrelations depend on the observables and should be monitored for all the relevant quantities in order to fully control the systematics in the simulations. For our runs at $\beta = 2.25$ we changed the MC integrator parameters to keep the plaquette autocorrelation time roughly constant, which is why the data in Table IVC do not show the same increase in autocorrelation times.

V. BENCHMARK MESONIC OBSERVABLES

Phenomenological results on the spectrum of the T2 theory are extracted from the study of lattice two-point functions. In this study we do not attempt to perform an investigation of the phenomenology of this theory, which will be presented in a forthcoming paper. Our aim is to provide lattice results useful as a benchmark for future investigations and to define the observables and the analysis procedure that we use here and in subsequent papers. In this section we describe in detail the procedure used to extract mesonic observables, such as the mass of the pseudoscalar or vector mesons, and the corresponding results on small lattices at $\beta = 2.0$.

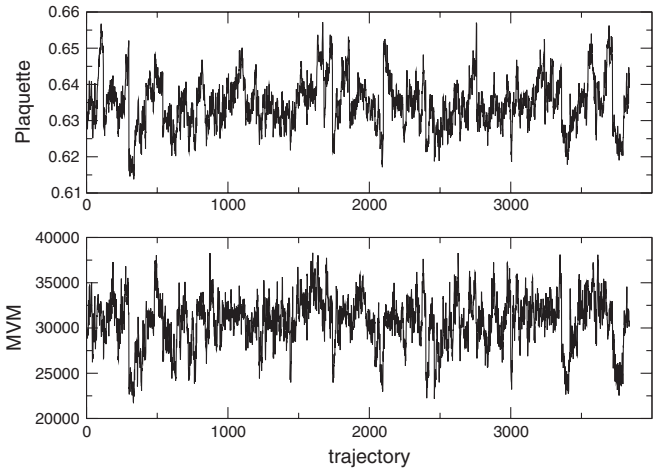

FIG. 8. Time histories for the plaquette and the solver number for the T2-B11 lattice at $\beta = 2$.

A. Definitions

Let Γ and Γ' be two generic matrices in the Clifford algebra, and we define the two-point correlator at zero momentum as follows:

$$f_{\Gamma\Gamma'}(t) = \sum_{\mathbf{x}} \langle \bar{\psi}_1(\mathbf{x}, t)\Gamma\psi_2(\mathbf{x}, t)\bar{\psi}_2(0)\Gamma'\psi_1(0)\rangle, \qquad (57)$$

where ψ_1 and ψ_2 represent two different flavors of degenerate fermion fields, so that we only consider flavor nonsinglet bilinears. Denoting the space-time position $(\mathbf{x}, t)$ by

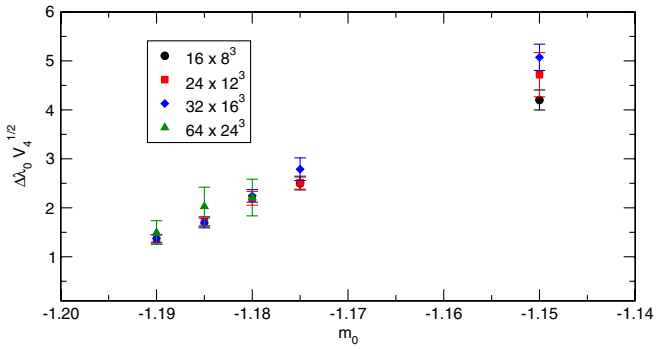

FIG. 9 (color online). The distribution width $\Delta\lambda_0$ of the lowest eigenvalue of the Dirac operator scales like $V^{-1/2}$. Results for $\beta = 2.25$.

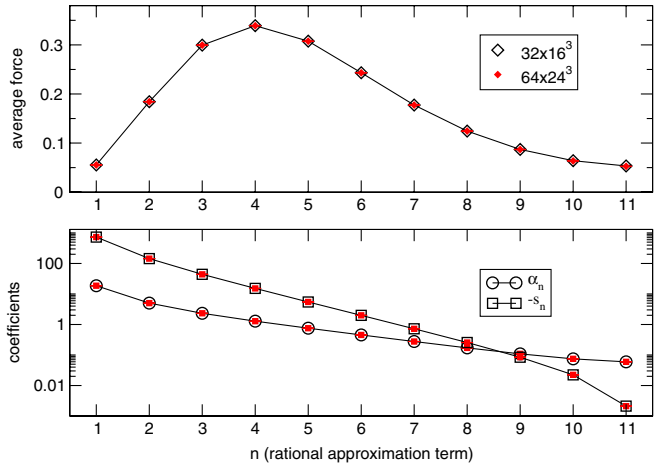

FIG. 10 (color online). Volume dependence of the average MC forces for each term in the rational approximation (upper panel) and average value of the approximation coefficients (lower panel). Data are obtained on the T2-E2 and T2-F0 lattices. Error bars in all cases are much smaller than the size of the symbols.

x and performing the Wick contractions yields

$$\langle \bar{\psi}_1(x)\Gamma\psi_2(x)\bar{\psi}_2(0)\Gamma'\psi_1(0)\rangle = -\mathrm{tr}[\Gamma S(x)\Gamma' S(-x)] = -\mathrm{tr}[\Gamma S(x)\Gamma'\gamma_5 S^\dagger(x)\gamma_5].$$

In practice we invert the Hermitian Dirac operator $Q = \gamma_5 D$ by solving the equation

$$Q(x,y)_{AB}\eta_B^{\bar{A},0}(y) = \delta_{A,\bar{A}}\delta_{x,0}, \tag{58}$$

where capital Latin letters like $A = \{a, \alpha\}$ are collective indices for color and spin, and $\bar{A}$, $x = 0$ is the position of the source for the inverter. The inversion is performed using a QMR recursive algorithm with even-odd preconditioning of the Dirac operator, which is stopped when the residue is less than 10^{-8}. Using the solution η obtained from the inversion, the above correlator is reexpressed as

$$\langle \cdots \rangle = -\tilde{\Gamma}_{AB}\eta_B^{C,y}(x)\tilde{\Gamma}'_{CD}\eta_A^{D,y}(x)^*, \tag{59}$$

where $\tilde{\Gamma} = \gamma_5\Gamma$ and $\tilde{\Gamma}' = \gamma_5\Gamma'$.

Following Ref. [68], masses and decay constants for the pseudoscalar meson are extracted from the asymptotic behavior of the correlators f_{PP} and f_{AP} at large Euclidean time. The pseudoscalar mass and the vacuum-to-meson matrix element are obtained from the correlator of two pseudoscalar densities:

$$f_{\mathrm{PP}}(t) = -\frac{G_{\mathrm{PS}}^2}{M_{\mathrm{PS}}}\exp[-M_{\mathrm{PS}}t] + \cdots. \tag{60}$$

The meson mass is obtained by fitting the effective mass to a constant, while the coupling G_{PS} is extracted from the amplitude of the two-point function f_{PP}. For the precise definition of the effective mass and coupling, we refer the reader to Ref. [68]. On the other hand, the ratio

$$m_{\mathrm{eff}}(t) = \tfrac{1}{2}[(\partial_0 + \partial_0^*)f_{\mathrm{AP}}(t)]/f_{\mathrm{PP}}(t) \tag{61}$$

yields the PCAC mass m with corrections of $\mathcal{O}(a)$ for the unimproved theory. On the relatively small lattices that we have used in this study, it is difficult to isolate clearly the contribution from the lowest state, which dominates the large-time behavior of two-point correlators. Figure 12 illustrates the typical quality of the plateau that is fitted to extract the pion mass. The data on the plot correspond to the effective mass obtained from two f_{PP} two-point function, whose asymptotic behavior is governed by the mass of the lightest pseudoscalar meson. Lattices with a smaller time extent do not show such a clear plateau; for these smaller lattices the determination of the masses is affected

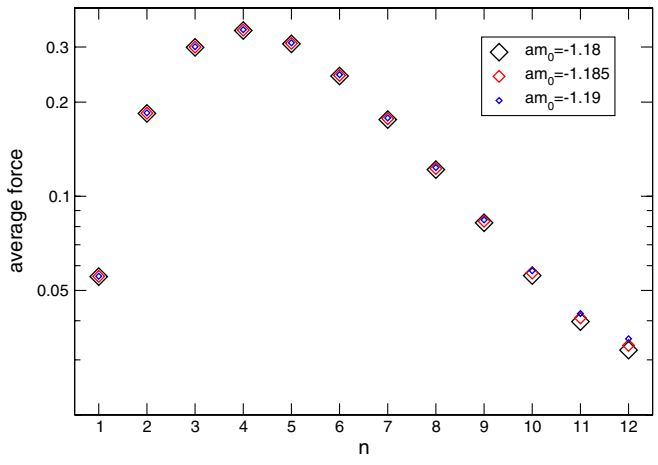

FIG. 11 (color online). Mass dependence of the average MC fermionic forces for each term in the rational approximation. Data are obtained on the T2-F lattices. Error bars are not shown as they are much smaller than the symbols used in the plot.

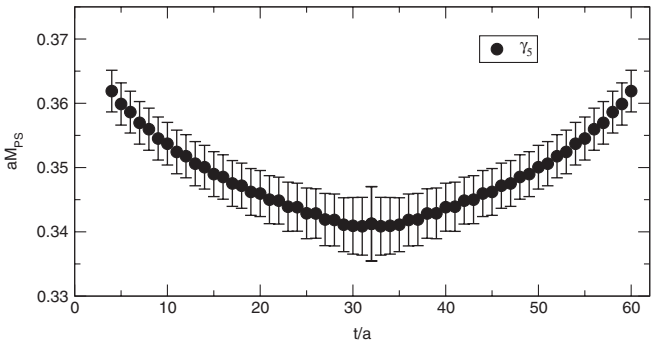

FIG. 12. Effective mass plot for the pion mass. The points correspond to the effective mass extracted from $f_{\mathrm{PP}}(t)$. The data refer to the T2-F0 lattice.

TABLE III. Results for the PCAC mass, for the pseudoscalar mass and coupling, for the vector meson mass and the pseudoscalar decay constant, from simulations on the T2-A lattices.

Lattice	am	$aM_{\rm PS}$	$a^2G_{\rm PS}$	$aM_{\rm V}$	$aF_{\rm PS}$
T2-A1	1.0199(14)	2.5711(12)	1.134(8)	2.5814(13)	0.3499(11)
T2-A2	0.7997(14)	2.2313(16)	1.277(10)	2.2516(17)	0.4102(16)
T2-A3	0.6718(14)	2.0212(19)	1.351(12)	2.0517(21)	0.4442(20)
T2-A4	0.5188(13)	1.7708(24)	1.435(14)	1.8222(26)	0.4748(26)
T2-A5	0.3129(23)	1.362(7)	1.356(34)	1.457(8)	0.4578(68)
T2-A6	0.2599(39)	1.196(18)	1.157(59)	1.280(20)	0.421(12)
T2-A7	0.1601(30)	0.868(27)	0.776(47)	0.901(31)	0.3301(97)
T2-A8	0.0921(16)	0.677(24)	0.607(27)	0.684(28)	0.2433(61)

by larger systematics due to the contamination from heavier states.

Note that the decay constant is not computed directly; it is obtained from the values computed above as

$$F_{\rm PS} = \frac{m}{M_{\rm PS}^2} G_{\rm PS}. \tag{62}$$

The decay constant extracted from bare lattice correlators is related to its continuum counterpart by the renormalization constant Z_A which has recently been computed in perturbation theory in Ref. [64].

Finally the mass of the vector state is extracted from the $f_{\rm VV}$ correlator, again following the procedure outlined in Ref. [68].

B. Results

A first set of results were obtained from runs on the T2-A lattices. Our results are summarized in Table III. The results obtained on such small lattices are affected by large systematic errors, and hence are not suitable for reliable phenomenology. On one hand, the limited extension of the T2-A lattices in the time direction means that it is virtually impossible to identify a proper plateau. As a consequence we estimate the mass of the relevant states from the value of the effective mass at the center of the lattice. For the heavier masses we find that our results are in agreement with the data presented in Ref. [25].[3] However, for these larger values of the bare mass, we see that all masses are $\mathcal{O}(1)$ in units of the inverse lattice spacing, and therefore we expect these results to be affected by large lattice artifacts. Smaller masses are needed in order to identify the chiral dynamics that is relevant for phenomenological studies. The lattices T2-A6, T2-A7, and T2-A8 yield smaller masses, but the lightest pseudoscalar meson has a mass $aM_{\rm PS} = 0.68$, which is still large in units of the UV cutoff. The study of the eigenvalue distributions presented in the previous section suggests that it is not possible to go to lighter masses on the T2-A lattices without entering the regime where the algorithm becomes unstable, or the system gets close to a phase transition.

[3]The reader may notice, however, that a different normalization for $aF_{\rm PS}$ has been used in Ref. [25]. The two choices differ by a factor of $\sqrt{8}$. Our choice for the normalization of $aF_{\rm PS}$ yields $F_\pi = 93$ MeV in QCD.

TABLE IV. Fitted values for the masses and vacuum-to-meson matrix element in lattice units for the T2-B lattices.

Lattice	am	$aM_{\rm PS}$	$a^2G_{\rm PS}$	$aM_{\rm V}$	$M_{\rm V}/M_{\rm A}$
T2-B7	0.2209(30)	1.149(11)	1.190(56)	1.269(12)	1.51(22)
T2-B8	0.1874(40)	1.044(18)	1.032(73)	1.163(20)	1.75(26)
T2-B9	0.1624(37)	0.952(19)	0.875(63)	1.067(21)	1.77(15)
T2-B10	0.1307(42)	0.838(29)	0.714(66)	0.952(30)	1.50(18)
T2-B11	0.0455(14)	0.356(34)	0.214(12)	0.366(43)	0.67(25)

The results obtained on the T2-B lattices for the pseudoscalar mass, the PCAC mass, the vector meson mass, the axial vector meson mass, and the vacuum-to-meson matrix element are reported in Table IV. As a result of the reduced width in the eigenvalue distribution, we can afford to simulate closer to the chiral limit, with a PCAC mass smaller than 0.1.

Several combinations of interest are also summarized in Table V: the ratio of the pseudoscalar mass squared to the PCAC mass, the bare pseudoscalar decay constant, and the mass of the vector meson in units of the pseudoscalar decay constant. They are computed from the primary observables discussed above, and the error propagation is done by the usual jackknife method. The main phenomenological conclusions of this paper are obtained from these values.

The computation of the pseudoscalar decay constant in the chiral limit is the method of choice to set the lattice scale. In a technicolor theory the decay constant is related to the vacuum expectation value of the Higgs field, and therefore $F_{\rm PS} = 250$ GeV. A realistic determination of the physical value of $F_{\rm PS}$ would be beyond the scope of this work. Here we simply report the values of $F_{\rm PS}$ in Tables III and V.

The ratio $M_{\rm V}/F_{\rm PS}$ is also an interesting quantity of a Technicolor theory. Our results for this quantity are summarized in Table V.

We stress again that the results in this section are only benchmarks: they are useful for checking future numerical

TABLE V. Fitted values for the relevant combinations of m, $M_{\rm PS}$, $G_{\rm PS}$, and $M_{\rm V}$ for the T2-B lattices. The value of the PCAC mass is reported again for clarity.

Lattice	am	$aM_{\rm PS}^2/m$	$aF_{\rm PS}$	$M_{\rm V}/F_{\rm PS}$
T2-B7	0.2209(30)	5.98(14)	0.399(14)	3.19(12)
T2-B8	0.1874(40)	5.82(24)	0.354(20)	3.29(19)
T2-B9	0.1624(37)	5.58(26)	0.314(18)	3.40(20)
T2-B10	0.1307(42)	5.30(41)	0.266(21)	3.58(30)
T2-B11	0.0455(14)	2.79(39)	0.154(8)	2.38(31)

simulations but not to draw any solid phenomenological conclusion about this theory.

VI. CONCLUSIONS

In this paper we have described the generalization of the HMC and RHMC algorithms to the case of generic representations of the color group SU(N). We have developed a general framework that can deal with Wilson fermions in arbitrary representations and generic number of colors N. We have put the emphasis on describing in detail the algorithmic issues that need to be faced in generalizing existing code to arbitrary representations. Since simulations for these new theories are still in their infancy, and even the simplest results are not known *a priori*, numerous independent studies will be welcome. We have provided an extensive number of tests of the algorithm and a detailed study of its behavior for the SU(2) gauge theory with fermions in the adjoint representation. Our benchmark results are ideally suited for validating lattice simulations of theories with fermions in higher representations.

We have presented benchmark results on small $8^3 \times 16$ lattices, giving full details of the procedure we used, so as to make all the results presented in this work reproducible beyond any ambiguity. On these small lattices, our results should be easily reproducible without any major investment of computational resources. We provided a large number of benchmark quantities, ranging from the average value of the plaquette to mesonic observables.

The results in this paper are the first step in a more comprehensive program that aims to study nonperturbative phenomena beyond QCD. Robust results for the spectrum and decay constants in technicolor theories are an important ingredient to search for strongly interacting BSM physics at the LHC. The techniques that have been developed for QCD offer all the theoretical and algorithmic tools needed to develop a comprehensive study of technicolor on the lattice. Lattice results will be important in order to test these theories as potential candidates for BSM physics. We stress again that an uncompromising theoretical formulation is mandatory for such studies that are investigating unknown theories in order to have some real predictive power. First numerical results should be benchmarked carefully against each other in order to verify that systematics are under control.

It is worthwhile to emphasize once again that the algorithmic framework that we have developed here can be readily used to study the planar orientifold equivalence and lattice supersymmetry. Preliminary results in this direction have already appeared [14].

ACKNOWLEDGMENTS

During the long gestation of this work, we have enjoyed discussing its progress with many people. We want to thank Adi Armoni, Francis Bursa, Simon Catterall, Biagio Lucini, Martin Lüscher, Francesco Sannino, Misha Shifman, and Gabriele Veneziano for discussions about various aspects of this work. L. D. D. acknowledges the kind hospitality of the Isaac Newton Institute, CERN, and Odense University while this work was progressing. Workshops at the INI, the Niels Bohr Institute, and Edinburgh provided a lively atmosphere for discussions. We thank SUPA for funding the workshop in Edinburgh. L. D. D. is funded by STFC. The work of C. P. has been supported by Contract No. DE-AC02-98CH10886 with the U.S. Department of Energy during the initial stages of this work. A. P. is supported by an STFC special project grant and by the ''Fondazione Angelo Della Riccia.''

APPENDIX A: GROUP-THEORETICAL FACTORS

The normalization of the generators in a generic representation R of SU(N) is fixed by requiring that

$$[T_R^a, T_R^b] = \mathrm{i} f^{abc} T_R^c, \tag{A1}$$

where the structure constants f^{abc} are the same in all representations. We define

$$\mathrm{tr}_R(T^a T^b) = \mathrm{tr}(T_R^a T_R^b) = T_R \delta^{ab}, \tag{A2}$$

$$\sum_a (T_R^a T_R^a)_{AB} = C_2(R)\delta_{AB}, \tag{A3}$$

and hence

$$T_R = \frac{1}{N^2 - 1} C_2(R) d_R, \tag{A4}$$

where d_R is the dimension of the representation R. The quadratic Casimir operators may be computed from the Young tableaux of the representation of SU(N) by using the formula

$$C_2(R) = \frac{1}{2}\left(nN + \sum_{i=1}^{m} n_i(n_i + 1 - 2i) - \frac{n^2}{N}\right), \tag{A5}$$

where n is the number of boxes in the diagram, i ranges over the rows of the Young tableau, m is the number of rows, and n_i is the number of boxes in the ith row.

The quantities d_R, T_R, and $C_2(R)$ are listed in Table VI for the fundamental, adjoint, 2-index symmetric, and 2-index antisymmetric representations.

TABLE VI. Group invariants used in this work.

R	d_R	T_R	$C_2(R)$
Fund	N	$1/2$	$(N^2-1)/(2N)$
Adj	N^2-1	N	N
2S	$N(N+1)/2$	$(N+2)/2$	$C_2(F)2(N+2)/(N+1)$
2AS	$N(N-1)/2$	$(N-2)/2$	$C_2(F)2(N-2)/(N-1)$

APPENDIX B: TWO-INDEX REPRESENTATIONS

The Hermitian generators T_F^a for the fundamental representation used are of the following form. For each pair of integers $1 \le k < l \le N$, we define two generators as

$$(T_F^{ij,+})_{mn} = \tfrac{1}{2}(\delta_{mk}\delta_{nl} + \delta_{ml}\delta_{nk}), \tag{B1}$$

$$(T_F^{ij,-})_{mn} = \frac{i}{2}(\delta_{mk}\delta_{nl} - \delta_{ml}\delta_{nk}), \tag{B2}$$

and for each $1 \le k < N$ one more generator is defined as

$$(T_F^k) = \frac{1}{\sqrt{2k(k+1)}}\mathrm{diag}(\underbrace{1, 1, \ldots, -k}_{k+1 \text{ terms}}, 0, \ldots, 0). \tag{B3}$$

The generators T_F^a are normalized so that $T_F = 1/2$. The generators for the other representations are obtained as follows.

We first give the explicit form for the representation functions R which map $U \to U^R$. We define for each representation an orthonormal base e_R for the appropriate vector space of matrices.

For the adjoint representation we define the base e_{Adj} for the $N \times N$ traceless Hermitian matrices to be $e^a_{\mathrm{Adj}} = T_F^a/\sqrt{T_F}$, $a = 1, \ldots, N^2 - 1$ (i.e. proportional to the generators of the fundamental representation and normalized to 1).

For the two-index symmetric representation the base $e_S^{(ij)}$, with $i \le j$, for the $N \times N$ symmetric matrices is given by

$$i \ne j, \qquad (e_S^{(ij)})_{kl} = \frac{1}{\sqrt{2}}(\delta_{ik}\delta_{jl} + \delta_{jk}\delta_{il}), \tag{B4}$$

$$i = j, \qquad (e_S^{(ii)})_{kl} = \delta_{ki}\delta_{li}. \tag{B5}$$

For the two-index antisymmetric representation the base $e_{\mathrm{AS}}^{(ij)}$, with $i < j$, for the $N \times N$ antisymmetric matrices is given by

$$(e_S^{(ij)})_{kl} = \frac{1}{\sqrt{2}}(\delta_{ik}\delta_{jl} - \delta_{jk}\delta_{il}). \tag{B6}$$

The maps R are explicitly given by

$$(R^{\mathrm{Adj}}U)_{ab} = U^{\mathrm{Adj}}_{ab} = \mathrm{tr}[e^a_{\mathrm{Adj}} U e^b_{\mathrm{Adj}} U^\dagger], \quad a, b = 1, \ldots, N^2 - 1, \tag{B7}$$

$$(R^S U)_{(ij)(lk)} = U^S_{(ij)(lk)} = \mathrm{tr}[(e_S^{(ij)})^\dagger U e_S^{(lk)} U^T], \quad i \le j, \quad l \le k, \tag{B8}$$

$$(R^A U)_{(ij)(lk)} = U^A_{(ij)(lk)} = \mathrm{tr}[(e_A^{(ij)})^\dagger U e_A^{(lk)} U^T], \quad i < j, \quad l < k. \tag{B9}$$

The generators T_R^a used are defined as the image of the generators in the fundamental under the differential of the maps R defined above: $T_R^a = R_* T_F^a$. Explicit expressions can easily be worked out from the definition above. The invariants T_R and $C_2(R)$ for the generators defined in this way are given in Table VI.

[1] M. Hasenbusch, Phys. Lett. B **519**, 177 (2001).
[2] M. Hasenbusch and K. Jansen, Nucl. Phys. **B659**, 299 (2003).
[3] M. Luscher, Comput. Phys. Commun. **165**, 199 (2005).
[4] L. Del Debbio, L. Giusti, M. Luscher, R. Petronzio, and N. Tantalo, J. High Energy Phys. 02 (2006) 011.
[5] C. Urbach, K. Jansen, A. Shindler, and U. Wenger, Comput. Phys. Commun. **174**, 87 (2006).
[6] M. A. Clark and A. D. Kennedy, Phys. Rev. Lett. **98**, 051601 (2007).
[7] S. Weinberg, Phys. Rev. D **13**, 974 (1976).
[8] L. Susskind, Phys. Rev. D **20**, 2619 (1979).
[9] C. T. Hill and E. H. Simmons, Phys. Rep. **381**, 235 (2003).
[10] F. Sannino, arXiv:0804.0182.
[11] A. Armoni, M. Shifman, and G. Veneziano, Nucl. Phys. **B667**, 170 (2003).
[12] D. B. Kaplan, Eur. Phys. J. Special Topics **152**, 89 (2007).
[13] L. Del Debbio, B. Lucini, A. Patella, and C. Pica, J. High Energy Phys. 03 (2008) 062.
[14] A. Armoni, B. Lucini, A. Patella, and C. Pica, Phys. Rev. D **78**, 045019 (2008).
[15] F. Sannino and K. Tuominen, Phys. Rev. D **71**, 051901 (2005).
[16] D. D. Dietrich and F. Sannino, Phys. Rev. D **75**, 085018 (2007).
[17] R. Foadi, M. T. Frandsen, T. A. Ryttov, and F. Sannino, Phys. Rev. D **76**, 055005 (2007).
[18] T. Banks and A. Zaks, Nucl. Phys. **B196**, 189 (1982).
[19] M. Luscher, R. Narayanan, P. Weisz, and U. Wolff, Nucl. Phys. **B384**, 168 (1992).
[20] T. Appelquist, G. T. Fleming, and E. T. Neil, Phys. Rev. Lett. **100**, 171607 (2008).
[21] Y. Shamir, B. Svetitsky, and T. DeGrand, Phys. Rev. D **78**, 031502 (2008).
[22] A. J. Hietanen, K. Rummukainen, and K. Tuominen, Phys. Rev. D **80**, 094504 (2009).
[23] F. Bursa, L. Del Debbio, L. Keegan, C. Pica, and T. Pickup, Phys. Rev. D **81**, 014505 (2010).

[24] A. Deuzeman, M. P. Lombardo, and E. Pallante, Phys. Lett. B **670**, 41 (2008).
[25] S. Catterall and F. Sannino, Phys. Rev. D **76**, 034504 (2007).
[26] S. Catterall, J. Giedt, F. Sannino, and J. Schneible, arXiv:0910.4387.
[27] S. Catterall, J. Giedt, F. Sannino, and J. Schneible, J. High Energy Phys. 11 (2008) 009.
[28] A. Hietanen, J. Rantaharju, K. Rummukainen, and K. Tuominen, Nucl. Phys. **A820**, 191c (2009).
[29] A. J. Hietanen, J. Rantaharju, K. Rummukainen, and K. Tuominen, J. High Energy Phys. 05 (2009) 025.
[30] F. Bursa, L. Del Debbio, L. Keegan, C. Pica, and T. Pickup, arXiv:0910.2562.
[31] A. Deuzeman, M. P. Lombardo, and E. Pallante, arXiv:0904.4662.
[32] Z. Fodor, K. Holland, J. Kuti, D. Nogradi, and C. Schroeder, J. High Energy Phys. 11 (2009) 103.
[33] Z. Fodor, K. Holland, J. Kuti, D. Nogradi, and C. Schroeder, Phys. Lett. B **681**, 353 (2009).
[34] Z. Fodor, K. Holland, J. Kuti, D. Nogradi, and C. Schroeder, arXiv:0911.2934.
[35] T. Appelquist, G. T. Fleming, and E. T. Neil, Phys. Rev. D **79**, 076010 (2009).
[36] T. Appelquist *et al.*, Phys. Rev. Lett. **104**, 071601 (2010).
[37] T. Appelquist *et al.*, Proc. Sci., CD09 (2009) 088.
[38] X.-Y. Jin and R. D. Mawhinney, Proc. Sci., LAT2009 (2009) 049.
[39] T. DeGrand, Y. Shamir, and B. Svetitsky, Phys. Rev. D **79**, 034501 (2009).
[40] T. DeGrand and A. Hasenfratz, Phys. Rev. D **80**, 034506 (2009).
[41] T. DeGrand, arXiv:0906.4543.
[42] T. DeGrand, Phys. Rev. D **80**, 114507 (2009).
[43] B. Svetitsky, Nucl. Phys. **A827**, 547c (2009).
[44] O. Machtey and B. Svetitsky, Phys. Rev. D **81**, 014501 (2010).
[45] A. Hasenfratz, Phys. Rev. D **80**, 034505 (2009).
[46] A. Hasenfratz, arXiv:0911.0646.
[47] D. K. Sinclair and J. B. Kogut, arXiv:0909.2019.
[48] J. B. Kogut and D. K. Sinclair, arXiv:1002.2988.
[49] E. Bilgici *et al.*, arXiv:0910.4196.
[50] L. Del Debbio, B. Lucini, A. Patella, C. Pica, and A. Rago, Phys. Rev. D **80**, 074507 (2009).
[51] C. Pica, L. Del Debbio, B. Lucini, A. Patella, and A. Rago, arXiv:0909.3178.
[52] B. Lucini, arXiv:0911.0020.
[53] M. Luscher, S. Sint, R. Sommer, and P. Weisz, Nucl. Phys. **B478**, 365 (1996).
[54] M. A. Clark and A. D. Kennedy, Nucl. Phys. B, Proc. Suppl. **129–130**, 850 (2004).
[55] S. Duane, A. D. Kennedy, B. J. Pendleton, and D. Roweth, Phys. Lett. B **195**, 216 (1987).
[56] T. Takaishi and P. de Forcrand, Phys. Rev. E **73**, 036706 (2006).
[57] A. Donini and M. Guagnelli, Phys. Lett. B **383**, 301 (1996).
[58] T. A. DeGrand and P. Rossi, Comput. Phys. Commun. **60**, 211 (1990).
[59] M. Luscher, Comput. Phys. Commun. **79**, 100 (1994).
[60] M. Creutz, Phys. Rev. D **38**, 1228 (1988).
[61] T. Takaishi, Comput. Phys. Commun. **133**, 6 (2000).
[62] S. Gupta, A. Irback, F. Karsch, and B. Petersson, Phys. Lett. B **242**, 437 (1990).
[63] B. Joo *et al.* (UKQCD), Phys. Rev. D **62**, 114501 (2000).
[64] L. Del Debbio, M. T. Frandsen, H. Panagopoulos, and F. Sannino, J. High Energy Phys. 06 (2008) 007.
[65] U. Wolff (ALPHA Collaboration), Comput. Phys. Commun. **156**, 143 (2004).
[66] H. B. Meyer *et al.*, Comput. Phys. Commun. **176**, 91 (2007).
[67] L. Del Debbio, G. M. Manca, and E. Vicari, Phys. Lett. B **594**, 315 (2004).
[68] L. Del Debbio, L. Giusti, M. Luscher, R. Petronzio, and N. Tantalo, J. High Energy Phys. 02 (2007) 082.